

CM²



MAGAZINE

第 31 期



南方科技大学海洋磁学中心主编

创刊词

海洋是生命的摇篮，是文明的纽带。地球上最早的生命诞生于海洋，海洋里的生命最终进化成了人类，人类的文化融合又通过海洋得以实现。人因海而兴。

人类对海洋的探索从未停止。从远古时代美丽的神话传说，到麦哲伦的全球航行，再到现代对大洋的科学钻探计划，海洋逐渐从人类敬畏崇拜幻想的精神寄托演变成可以开发利用与科学研究的客观存在。其中，上个世纪与太空探索同步发展的大洋科学钻探计划将人类对海洋的认知推向了崭新的纬度：深海（deep sea）与深时（deep time）。大洋钻探计划让人类知道，奔流不息的大海之下，埋藏的却是亿万年的地球历史。它们记录了地球板块的运动，从而使板块构造学说得到证实；它们记录了地球环境的演变，从而让古海洋学方兴未艾。

在探索海洋的悠久历史中，从大航海时代的导航，到大洋钻探计划中不可或缺的磁性地层学，磁学发挥了不可替代的作用。这不是偶然，因为从微观到宏观，磁性是最基本的物理属性之一，可以说，万物皆有磁性。基于课题组的学科背景和对海洋的理解，我们对海洋的探索以磁学为主要手段，海洋磁学中心因此而生。

海洋磁学中心，简称 CM^2 ，一为其全名“Centre for Marine Magnetism”的缩写，另者恰与爱因斯坦著名的质能方程 $E = MC^2$ 对称，借以表达我们对科学巨匠的敬仰和对科学的不懈追求。

然而科学从来不是单打独斗的产物。我们以磁学为研究海洋的主攻利器，但绝不仅限于磁学。凡与磁学相关的领域均是我们关注的重点。为了跟踪反映国内外地球科学特别是与磁学有关的地球科学领域的最新研究进展，海洋磁学中心特地主办 CM^2 Magazine，以期与各位地球科学工作者相互交流学习、合作共进！

“海洋孕育了生命，联通了世界，促进了发展”。21世纪是海洋科学的时代，由陆向海，让我们携手迈进中国海洋科学的黄金时代

目 录

海磁文苑	1
漫谈中美.....	1
岩石磁学演绎	4
第 21 章：交变场衰减率对 ARM 的影响	4
文献导读	7
1. 下地幔较高电导系数导致太平洋地区磁场变化减弱	7
2. 加拿大安大略省 18.8 亿年燧石铁建造中赤铁矿取代和氧化印 记	9
3. 混杂岩 vs.流体和熔体使弧地幔富集：利用钡同位素对 Tonga- Kermadec 弧熔岩进行的新测试	12
4. 一个晚白垩纪-始新世地磁极性年表 (MQSD20)：在多个洋中 脊侧翼具有稳定的扩张速率	14
5. 菲律宾海板块在日本下方发生分裂.....	16
6. 阿拉斯加中南部 Castle Mountain Fault 的地球物理研究	19
7. 东亚降雨 $\delta^{18}\text{O}$ 与多种季风指标的关系	21
8. 微生物铁还原过程对碳酸盐沉淀的影响	25
9. Azores 群岛熔岩流序列中最后一次地磁极倒转的火山记录	27
10. 东亚冬季风在早全新世减弱，中晚全新世增强	29

海磁文苑

漫谈中美

中美贸易战打了一年半了，打打谈谈，谈谈打打，对于彻底走向缓和我看近期不要报希望了。我觉得推特之王特朗普是决然不敢向伊朗开战的，不然他们的工作重心——中国问题又要像 20 年前那样偏离到中东去。以前高晓松讲中美之间，你中有我，我中有你，是不可能打起来的，现在打脸了。而他认为中俄之间边界问题，投资问题等注定是真正得敌对状态，又打脸了。国际上，真的就是达尔文主义，弱肉强食的状态。联合国越来越像国联，没有什么用处。小国叙利亚的土地上，美国、欧盟、俄罗斯、伊朗、土耳其等大中型国家及其代理人打来打去，流的是别人的血，跟日俄战争在东北打有什么区别，致使上千万叙利亚人成为难民，又有什么正义可言呢？

美帝

齐国名将司马穰苴讲：国虽大，好战必亡。其实说得多是大陆国家，像美帝这种大型海洋国家，好战真的未必能亡。你打不着他。美帝，世界上几乎每一个民族在她那儿都有五百万以上的人口，这种色彩缤纷的联邦帝国，必然创新力极强，精力极其旺盛，也难以短期衰败。将今论古，如今之美帝，可喻为新罗马帝国。大致相当于罗马帝国西移到了美洲，以前以地中海为内海，如今则以大西洋为内海，将西欧变为其附庸邦国。再看看加拿大和澳洲婢膝之嘴脸，这种现象更会在英国脱欧后愈加明显。古罗马帝国兴盛了 400 余年，存在了 1500 年，比之如今美帝不过 200 年，所以我们不用过于乐观美帝之衰败。

中国

中国呢，我们是中土之国，其实如果早一点知道六千年地中海文明的话，我们只能算是东方之国。与古罗马并称时的帝国，是西汉。有估计说，西汉鼎盛时期综合国力达到罗马帝国之八成，我觉得这个说法靠谱。中国人勤劳踏实，但民族和性格单一，创新力较差。虽海陆兼备，但海防塞防压力均在咫尺。如果能妥善经营，整体实力能保持在古罗马帝国/美帝之八十分水平，应该就算是复兴了。

其实还有一个更牛的朝代，那就是唐朝。唐朝之影响，北至贝加尔湖，西至伊朗，东到日本。国内开明到任用外国人做相国，实力盛极一时。包括文化在内的综合国力都能达到或超越古罗马帝国/美帝的体量。但是如今中古农耕时期已过，而且唐朝鼎盛时期昙花一现，

不及西汉文景武昭宣五帝之绵长。况且如今西有中东乱做一团，北有光脚毛熊，不可比之。

如今之中国，GDP 比之美帝三分有其二，PPP 则高出美帝二成，国力可以说来到了西汉武帝初年，如果治法得当，时运又好的话，还有百年兴旺可能。近期有上海学者写了两本书，一曰汉武盛世，一曰康乾盛世，比之本朝，喻义清之克复台湾，重光先汉之兴隆。有人觉得兴奋，有人说是舔痔，各执其词。其实万言不值一杯水，富强了，瞎逼逼都没有意义。

人权

人权，西方喜欢讲人权。比如西方觉得苏联侵犯东欧国家人权，可是苏联民主化解体成俄罗斯时，为什么不接受她呢？因为她还不够小，还有威胁。你看南斯拉夫解体了，我欧盟不就照单全收了嘛。西方屠杀犹太人，完事又觉得犹太人可怜，就让犹太人跑到阿拉伯的地盘上建国，至今已经快吞并整个巴勒斯坦了。犹太人的人权保住了，巴勒斯坦呢？西方第一时间只拍香港警察打暴徒，可是加泰罗尼亚要独立时，西班牙的出手有多少西媒关注？印度在克什米尔戒严，欺负穆斯林居民，但西方依旧毅然决然围着香港问题天天报道。偶尔在谈及克什米尔问题时，竟然还能生扯出中国的新疆问题来，也真是服了。香港暴徒用伞头袭击警车，警察出来抵抗，结果西方记者们第一时间从警察后面包抄，举着摄像头挡住警察的退路，呵呵了。

你在国外呆的越久，越能理解西方的“人权”。你会发现，西方枪击没人管，东方稍微骂骂人，友邦便会“莫名惊诧”！这里的游行示威，都要提前申请备案，过关的才行，不过关的非法。看来看去，我终于明白，一切都是“秀”！是领导者也就是未来政客的一场个人“秀”，是跟从者也就是一般平民不想工作享受生活的派对“秀”。但我相信不论每个国家大部分都是好人，只有那些精力旺盛的政客和记者，操纵着客观的国家机器惹是生非，秀自己的存在感，激发过分的民族主义，这真不是好事。

近代

昔日民国治下的三十八年，东北丢了不敢开战，辛丑赔款赔日本能赔到全面抗战第三年，新疆半独立，西藏几乎完全独立，全民抗战发动无能，无怪被世界看贬。改革开放连续发展 40 年后，也有人可能不理解现在我们做法，希图能再闷声发大财，多年后再说说话，而不应该有中国制造 2025、南海造岛，提出一带一路、亚投行等世界级口号，公然对抗美帝。其实君不见越南、菲律宾早已在南沙填海多年，未见西方自由媒体报道；君不见美帝早已从高科技着手制裁中国，军事武器禁运。与其等到躲无可躲，不如今日挺然入局，正是我们共和国的气魄。

中美

中庸之道，尽善尽美。一头一尾的“中”和“美”都是极好的词。中美之间，最好还是和朝鲜战场一样，你打你的，我打我的，各自为战的好，最后多半还是一个平手。

葛坤朋

2019年10月于爱丁堡

岩石磁学演绎

第 21 章：交变场衰减率对 ARM 的影响

ARM 并不是一个简单的参数，它除了受到磁性颗粒的粒径变化、磁相互作用的影响外，AF 的衰减率也对 ARM 有显著影响(Yu et al., 2003)。通过对合成以及天然样品的研究发现，对于 SD 颗粒，随着 AF 衰减率增加，其获得的 ARM 值会降低大约 10%。对于 PSD 颗粒，ARM 降低的幅度会减小到大约 5%。MD 颗粒具有完全相反的趋势，随着 AF 衰减率的增加，其获得的 ARM 会升高。这个特性可以被用来区分 SD 和 MD 颗粒。

磁性颗粒获得的 ARM 与其磁畴状态密切相关。对于 SD 颗粒来说，降低 AF 衰减率等同于延长了 AF 场对颗粒的作用时间，这样颗粒更能够达到平衡状态，从而获得更高的剩磁。而对于 MD 颗粒而言，较小的 AF 衰减率使得其内部的自发退磁过程更充分，从而降低了总体的剩磁。

上述实验证实,不同型号的 ARM 仪器，其 AF 衰减率不会完全相同，也就是说，不同仪器上测量的 ARM，即使已经归一化成 χ_{ARM} ，也可能无法实现对比。

Yu et al. (2003)从理论上进一步研究了 ARM 的 AF 衰减率特性。

ARM 与 TRM 具有一定的可比性，因此，

$$M_{ARM} / M_{rs} = 2 \ln(f_0 t) H / H_{K0}$$

其中 H_{K0} 是室温的 H_K 。

$$t = [kT_0 / \Delta E(T_0)] [H_{K0} / (-dH/dt)]$$

可见，ARM 的获得与 AF 场的衰减速率反相关，AF 场衰减得越慢，越能获得大的 ARM 值。

Liu et al.(2004)利用了 ARM 与 AF 衰减率的关系研究了中国塬堡剖面黄土-古土壤 L2-S1-L1 序列样品的粒径分布。定义

$$\chi_{ARM.DR} \% = (\chi_{ARM.2} - \chi_{ARM.20}) / \chi_{ARM.2} \%$$

研究结果表明, 大部分样品的 $\chi_{ARM.DR} \%$ 在 8%-10%, 说明 ARM 确实以 SD 颗粒占主导。此外, $\chi_{ARM.DR} \%$ 与成土作用的强弱关系不大, 说明成土作用产生的 SD 颗粒的粒径分布很稳定, 与成土作用强弱无关。Liu et al.(2004)进一步对比了 $\chi_{ARM.DR} \%$ 与 χ_{fd} , 二者呈显著线性相关。这说明从 SP 到 SD 的纳米颗粒范围内, 磁性矿物的粒径分布保持稳定, 其磁性变化主要由纳米颗粒的含量变化引起。因此, 对于该区的黄土-古土壤序列, χ_{fd} 和 ARM 可以认为是 SP 和 SD 颗粒含量的替代指标。

尽管 ARM 与 TRM 在理论上有一定的可比性, 但是对于不同磁畴状态的颗粒, 其 ARM 与 TRM 并不完全一样。具体来说, 对于粒径大于 $2 \mu\text{m}$ 的颗粒, 其 χ_{TRM}/χ_{ARM} 比值与粒径弱相关。但是对于 200 nm 左右的 PSD 样品, 其比值可大于 10。

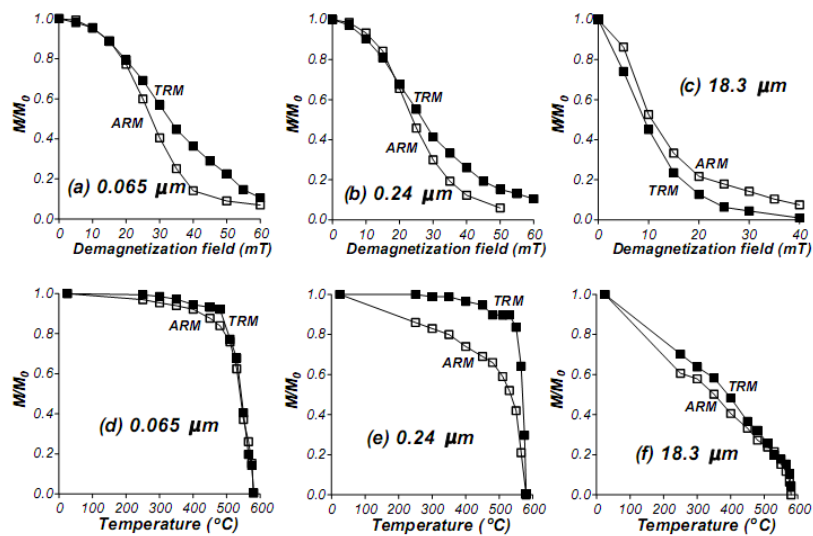


图 1 不同粒径磁铁矿的 ARM 与 TRM 的交变退磁谱(a-c)与热退磁谱(d-f) (Yu et al., 2003)。

ARM 与 TRM 还具有相似的交变退磁曲线, 只是 SD/PSD 颗粒的 TRM 比 ARM 稍“硬”些。 Yu et al. (2003) 利用合成样品及天然样品对二者的热退磁性质进行了研究 (图 1), 发现对于单畴颗粒(SD)和多畴颗粒(MD), 其 ARM 与 TRM 的热退磁曲线几乎一致; 而假单畴颗粒(PSD) 的 TRM 明显比 ARM“硬”, 这可能是 PSD 中 ARM 和 TRM 二者的微观结构不同造成的。粒径大小对 TRM/ARM(R 比值) 有着很强的影响, 合成样品中, 粒径为 $0.2\ \mu\text{m}$ 时, R 比值最大, 更有趣的是合成样品的 R 比值要比天然样品的更“陡”些。

文献导读

1. 下地幔较高电导系数导致太平洋地区磁场变化减弱



Mathieu Dumberry and Colin More., Weak magnetic field changes over the Pacific due to high conductance in lowermost mantle [J]. Nature Geoscience, 13, 7, 516-520.

<https://doi.org/10.1038/s41561-020-0589-y>

摘要: 过去几个世纪里, 地球磁场在太平洋地区的时间变化是异常的低。其原因与靠近地核-地幔边界的液态外核中大规模的流体流动有关。太平洋下部流动更弱, 表现为一个行星尺度的偏心环流大范围避开该区域。然而, 是什么调控这种流动方式的特征还未可知。因此, 作者提供了一个关于地球核心动力学的数值模拟的结果, 其中包括电磁耦合与地幔底部的非均匀性导电层。结果显示, 当该层位的导电性比太平洋下部其他区域都很高时, 较大的电磁阻力会削弱局部核心流, 并使行星环流偏离太平洋区域。下地幔导电性的性质仍然不清楚, 但是地核-地幔边界的地形波动中圈闭的层状核流体是一种可能的解释。

ABSTRACT: For the past few centuries, the temporal variation in Earth's magnetic field in the Pacific region has been anomalously low. The reason for this is tied to large-scale flows in the liquid outer core near the core-mantle boundary, which are weaker under the Pacific and feature a planetary-scale gyre that is eccentric and broadly avoids this region. However, what regulates this type of flow morphology is unknown. Here we present results from a numerical model of the dynamics in Earth's core that includes electromagnetic coupling with a non-uniform conducting layer at the base of the mantle. We show that when the conductance of this layer is higher under the Pacific than elsewhere, the larger electromagnetic drag force weakens the local core flows and deflects the flow of the planetary gyre away from the Pacific. The nature of the lowermost mantle conductance remains unclear, but stratified core fluid trapped within topographic undulations of the core-mantle boundary is a possible explanation.

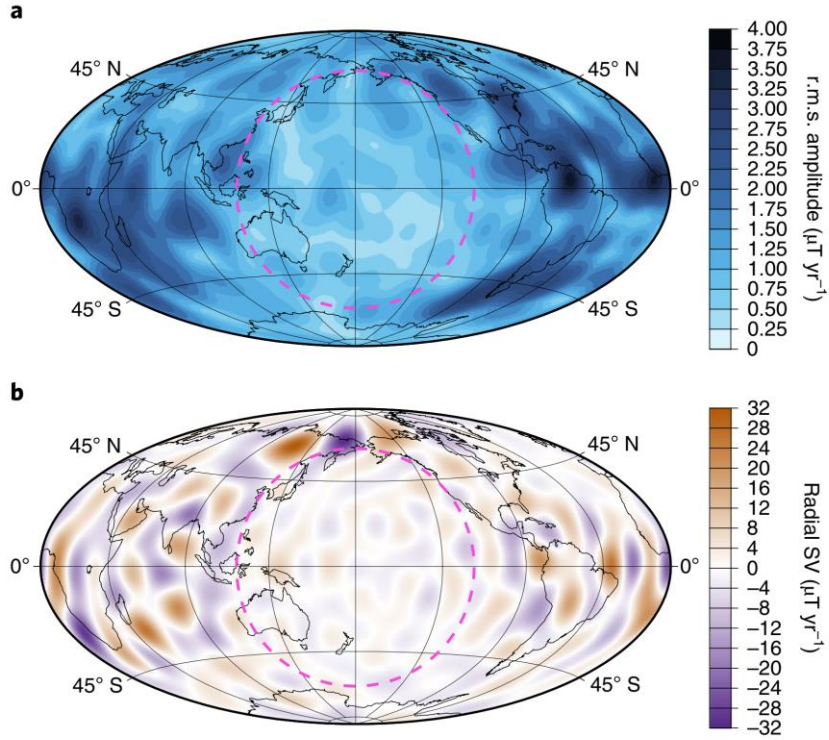


Figure 1. The low geomagnetic secular variation in the Pacific. a, The mean intensity of the radial component of the SV at the CMB, jB_{rj} , over the time period 1590-1990 from the gufm field model4. The r.m.s. amplitude of jB_{rj} in the Pacific (pink dashed circle) is $796.32 \text{ nT yr}^{-1}$ while the global average is $1,332.86 \text{ nT yr}^{-1}$, for a ratio of 0.5975. b, The radial component of the SV at the CMB, B_r , in 2015 from the CHAOS-6 field model8 truncated at spherical harmonic degree 16. The r.m.s. amplitude of jB_{rj} over the Pacific (pink dashed circle) is $2,034.13 \text{ nT yr}^{-1}$ while the global average is $4,401.09 \text{ nT yr}^{-1}$, for a ratio of 0.4622.

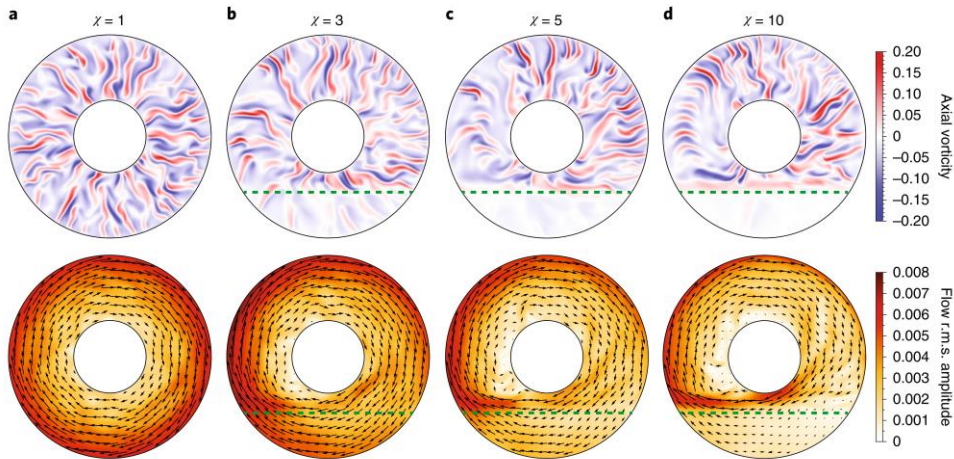


Figure 2. Modification of core flows by a non-uniform EM drag at the CMB. a–d, Snapshots of the axial vorticity (top row) and time-averaged flow maps (bottom row; colour scale indicates flow speed, arrows show direction) from our quasi-geostrophic model for $Ra = 5 \times 10^8$, $Pm = 0.1$ and $X = 1$ (a), 3 (b), 5 (c) and 10 (d). All plots are equatorial planforms. The Pacific region is shown in the bottom section of each planform, in the same location as in Fig. 2, and is delimited by a dashed green line in b, c and d. The colour scales on the right are common to all four panels and are in non-dimensional units.

2. 加拿大安大略省 18.8 亿年燧石铁建造中赤铁矿取代和氧化印记



翻译人：蒋晓东 jiangxd@sustech.edu.cn

Rasmussen, B., Muhling, J. R., et al. *Hematite replacement and oxidative overprinting recorded in the 1.88 Ga Gunflint iron formation, Ontario, Canada [J]. Geology, 2020,48, 688-692.*

摘要：加拿大安大略省 18.8 亿年燧石铁建造在建立沉积铁建造模型方面具有重要意义。富含赤铁矿铁建造夹杂燧石叠层石被认为含有丰富的蓝藻化石，由此认为微生物驱动了 Fe^{2+} 氧化与沉积。尽管燧石铁建造中具有丰富的赤铁矿，然而其主要的来源机制还不清楚。本研究在贯穿燧石建造的钻孔中给出了铁硅酸盐颗粒被赤铁矿取代的证据。铁氧化物取代从颗粒边界向内，并且沿着颗粒间裂隙，形成了以铁硅酸盐为核的铁氧化物富集边。页岩铁建造中丰富的有机质暗示富铁泥岩经历过厌氧成岩作用，共存的赤铁矿并不是直接沉积，而是埋藏后形成。广泛存在的蚀变结构指示大多数的赤铁矿并不是同沉积形成。这个氧化印记揭示富铁沉积初始来自还原的富 Fe^{2+} 的矿物。研究结果暗示假设微生物驱动铁氧化沉积的经典模型可能是有瑕疵的。该研究同时也使一些问题浮现，例如赤铁矿在其他铁建造中的来源以及微生物在早期海洋中铁沉积的作用等。

ABSTRACT: The 1.88 Ga Gunflint Formation in Ontario, Canada, has played a key role in the development of current models for the deposition of iron formations. The presence of hematite-rich iron formation intercalated with chert stromatolites containing purported cyanobacterial microfossils sparked the idea that biology was the principal driver of Fe^{2+} oxidation and iron deposition. However, despite the abundance of hematite in the Gunflint Formation, a primary depositional origin has not been established. Here we present evidence for the replacement of Fe-silicate granules by hematite in drill core intersecting the Gunflint Formation. Iron-oxide replacement proceeded inwards from granule boundaries and along intergranular fractures, producing iron oxide-rich rims around Fe-silicate cores. The abundance of organic matter in shaly iron formation implies that the iron-rich mudstones experienced anoxic diagenesis and that coexisting hematite was not depositional but formed after burial. Widespread distribution of the alteration textures indicates that this was a large-scale process and that much of the hematite is not primary. Lifting the veil of oxidative overprinting reveals an iron-rich sediment that was originally more reduced and dominated by Fe(II)-rich minerals. Our results imply that a major assumption

underpinning the original model for biological iron oxidation as the driver of iron formation deposition may be flawed, raising broader questions about the origin of hematite in other iron formations and the role of biology in iron deposition in the early oceans.

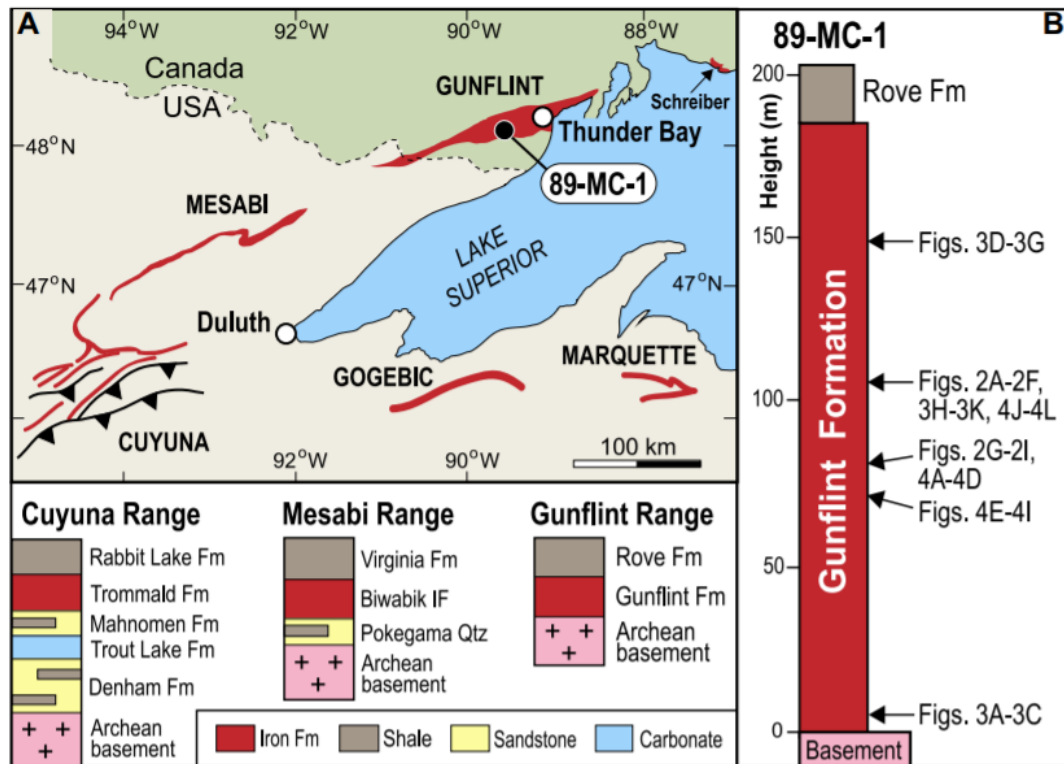


Figure 1. a, Locality map and simplified stratigraphic columns for Lake Superior iron formations (Ontario, Canada, and north-central United States), including Cuyuna, Mesabi, and Gunflint Ranges. Fm-Formation; IF-Iron Formation; Qtz-Quartzite. b, Stratigraphic column of drill hole 89-MC-1 showing locations of samples from Gunflint Formation.

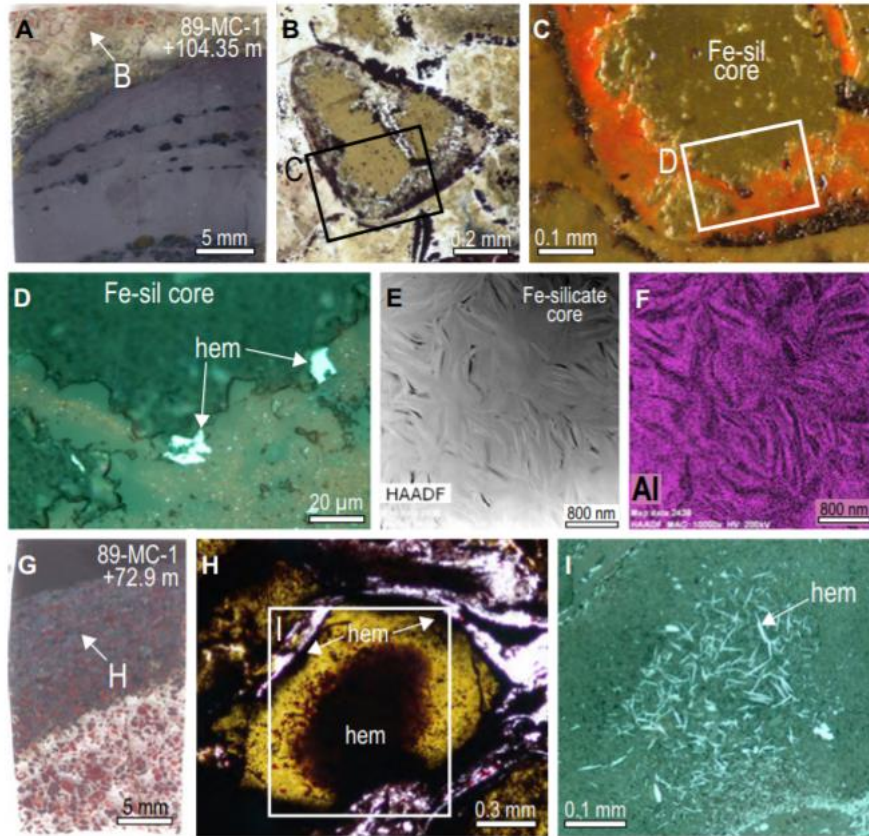


Figure 2. Photomicrographs of iron-silicate granules partially replaced by hematite from drillhole 89-MC-1 (Poulton et al. 2010). a, Scanned polished thin section showing hematite-rich mudstone and chert-cemented granule bed (top). b, Plane polarized light (PPL) image of granule with Fe-silicate core (green) and hematite-rich rim (black) in chert bed. c, Incident light image of granule showing fine-grained hematite particles (red) in granule rim. d, Reflected light (RL) image of interface between Fe-silicate (Fe-sil) core and chert with abundant hematite “dust” particles and two larger hematite crystals (hem). e, Highangle annular dark field (HAADF) scanning transmission electron microscopy (STEM) image of very fine-grained Fe-silicate minerals in transmission electron microscope (TEM) foil cut from core of green granule. f, TEM energy dispersive X-ray spectrometer (EDS) element map of aluminum (Al) for region in E. g, Scanned polished thin section of chert-cemented granule bed (bottom), compacted granule bed (center), and hematite-bearing mudstone (top). h, PPL image of Fe-silicate granule (green) with hematite-rich core and rim (see arrows). i, RL image of granule core (inset in H) showing randomly oriented hematite plates (white) in Fe-silicate core.

3. 混杂岩 vs. 流体和熔体使弧地幔富集：利用钡同位素对 Tonga-Kermadec 弧熔岩进行的新测试



翻译人：冯婉仪 fengwy@sustech.edu.cn

Wu F, Turner S, Schaefer B F. *Mélange versus fluid and melt enrichment of subarc mantle: A novel test using barium isotopes in the Tonga-Kermadec arc*[J]. *Geology*, 2020, <https://doi.org/10.1130/G47549.1>.

摘要：在过去的几年中，所谓的混杂岩模型被作为一种用来替代长期存在的由俯冲板块释放的流体和沉积物组分分别进入弧地幔并使其富集的模式。在混杂岩模型中，来自俯冲板块的组分在板片-地幔交界面发生物理混合。混杂岩物质会以底辟体的形式上升至地幔楔更热的区域并与地幔岩发生混合，随后，这些混合的地幔岩会发生部分熔融。在这里，我们首次对 Tonga-Kermadec 弧（西南太平洋）的火山熔岩进行了 Ba 同位素研究，并且表明 Ba 同位素可以区分来自不同俯冲组分的流体和熔体。这为争议提供了新的限制。我们观察到 Ba 同位素沿走向显著的变化，这可以由来源于俯冲板块的沉积物和蚀变洋壳（AOC）流体以不同的比例添加至地幔源区来解释。Ba-Sr-Pb 同位素的关系表明，沉积物熔体和 AOC 流体分别在不同的时间里添加到弧熔岩的源区中。这与混杂岩模型不一致，至少在这个弧中是这样的。

ABSTRACT: In the past few years, the so-called *mélange* model has been offered as an alternative to the long-standing model of enrichment of the subarc mantle by separate additions of fluid and sediment components from the subducting plate. In the *mélange* model, components from the subducting plate become physically mixed at the slab-mantle interface. Partial melting of the peridotite subsequently occurs after being hybridized by the *mélange* material that diapirically rises into hotter portions of the wedge. Here, we present the first Ba isotope study of lavas from the Tonga-Kermadec arc (southwest Pacific Ocean) and show that Ba isotopes distinguish between fluid and melt derived from different subducted components. This provides fresh constraints on the debate. Remarkable along-strike Ba isotope variations were observed and are best explained by contributions from variable proportions of sediment and altered oceanic crust (AOC) fluid from the subducting plate. Combined Ba-Sr-Pb isotope relationships indicate that sediment melt and AOC fluid were added to the source of the arc lavas separately at different times. This is inconsistent with the *mélange* model, at least in this arc.

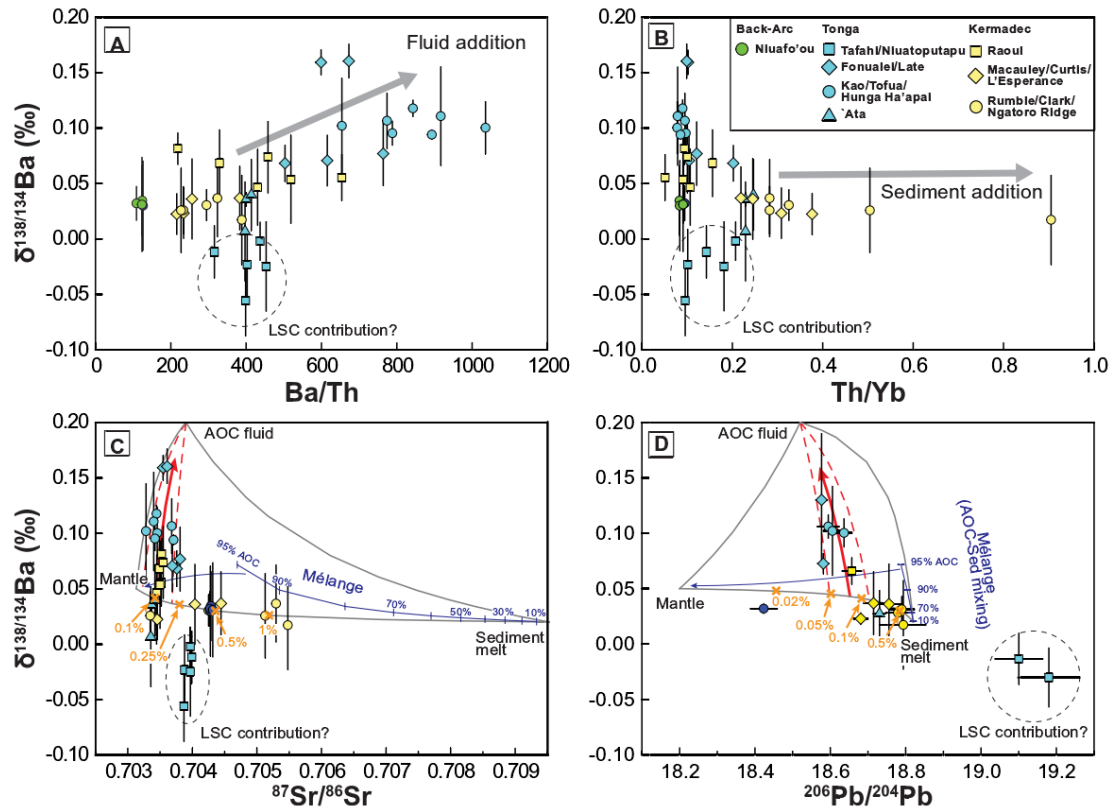


Figure 1. Correlations between $\delta^{138/134}\text{Ba}$ and (A) Ba/Th, (B) Th/Yb, (C) $^{87}\text{Sr}/^{86}\text{Sr}$, and (D) $^{206}\text{Pb}/^{204}\text{Pb}$. LSC—Louisville Seamount Chain. Error bars for $\delta^{138/134}\text{Ba}$ in A, B, and C represent 2 standard deviations (SD). Plots in D show the average $\delta^{138/134}\text{Ba}$ versus average $^{206}\text{Pb}/^{204}\text{Pb}$ for each island (on the Tonga-Kermadec arc, southwest Pacific Ocean) based on our $\delta^{138/134}\text{Ba}$ data and literature double-spike Pb isotope data (Table S2 [see footnote 1]). In C and D, solid curves represent calculated mixing lines among mantle, sediment melt, and altered oceanic crust (AOC) fluid; crosses denote the proportion of sediment addition in %; red lines and arrow represent the calculated mixing line between mantle metasomatized by sediment melt and AOC fluid; blue line shows calculated *mélange* component derived from a range of plausible bulk mixing of AOC and sediment; and blue arrow depicts the mixing trend of *mélange* and wedge peridotite. Details of the modeling calculations can be found in the Supplemental Material (see footnote 1).

4. 一个晚白垩纪-始新世地磁极性年表 (MQSD20) : 在多个洋中脊侧翼具有稳定的扩张速率

翻译人:李园洁 liyj3@sustech.edu.cn



Malinverno A, Quigley K W, Staro A, et al. *A Late Cretaceous-Eocene Geomagnetic Polarity Time Scale (MQSD20) that steadies spreading rates on multiple mid-ocean ridge flanks[J]. Journal of Geophysical Research: Solid Earth. 2020. doi:10.1029/2020jb020034*

摘要: 洋中脊侧翼的磁异常记录到地球磁场的倒转历史, 磁化洋壳的块体宽度结合绝对年龄可用来构建地磁极性年表 (GPTS)。目前的 GPTS 假定南大西洋的扩张速率平滑的变化, 本文将扩展到不同的扩张中心来更新晚白垩纪-始新世 (C33-C13, ~84-33 Ma) 的 GPTS。文中综合南太平洋 (23 条航迹线), 北太平洋 (35 条), 南大西洋 (33 条) 和印度洋 (55 条) 的磁异常航迹线。航迹线投影到板块构造流线上, 磁异常极性块体边界的距离通过蒙特卡洛计算方法迭代改变块体模型的距离和磁异常偏态角度与实测磁异常曲线的拟合来确定。然后每条航迹线得到的距离数据综合到 13 个洋中脊侧翼区域的块体模型距离中。最后利用另一种蒙特卡洛计算方法迭代极性时边界的年龄使得所有区域的扩张速率变化最小并且符合最新的放射性同位素年龄数据, 构建出最终的 MQSD20 GPTS。MQSD20 GPTS 的亮点是 50-45 Ma 期间一个重要板块运动的变化, 这个时间印度洋的扩张速率降低, 印度板块与欧亚板块碰撞, 而南大西洋和北太平洋扩张速率增加, 夏威夷-皇帝海山链方向发生改变。

ABSTRACT: Magnetic anomalies over mid-ocean ridge flanks record the history of geomagnetic field reversals, and the width of magnetized crustal blocks can be combined with absolute dates to generate a Geomagnetic Polarity Time Scale (GPTS). We update here the current GPTS for the Late Cretaceous-Eocene (chrons C33-C13, ~84-33 Ma) by extending to several spreading centers the analysis that originally assumed smoothly varying spreading rates in the South Atlantic. We assembled magnetic anomaly tracks from the southern Pacific (23 ship tracks), the northern Pacific (35), the southern Atlantic (33), and the Indian Ocean (55). Tracks were projected onto plate tectonic flow lines, and distances to magnetic polarity block boundaries were estimated by fitting measured magnetic anomalies with a Monte Carlo algorithm that iteratively changed block model distances and anomaly skewness angles. Distance data from each track were then assembled in summary sets of block model distances over 13 ridge flank regions. We obtained a final MQSD20 GPTS with

another Monte Carlo algorithm that iteratively perturbed ages of polarity chron boundaries to minimize the variability of spreading rates over all ridge flanks and fit an up-to-date set of radioisotopic dates. The MQSD20 GPTS highlights a major plate motion change at 50-45Ma, when spreading rates age decreased in the Indian Ocean as India collided with Eurasia while spreading rates increased in the South Atlantic and Northern Pacific and the Hawaii-Emperor seamount chain changed its orientation.

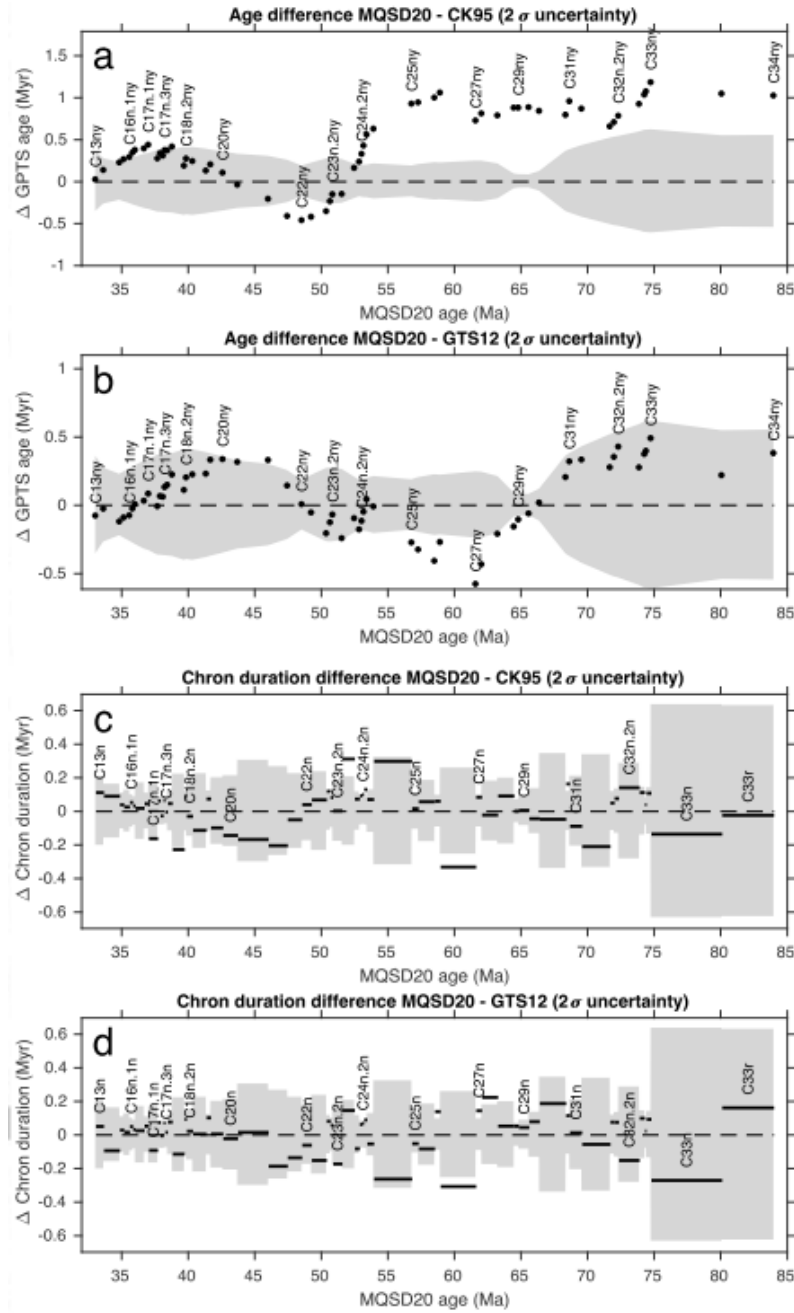


Figure 1. GPTS comparison between MQSD20, CK95, and GTS12. Differences in chron boundary ages are in (a) and (b); differences in chron durations are in (c) and (d). The shaded areas encompass the 2σ uncertainty of the MQSD20 GPTS.

5. 菲律宾海板块在日本下方发生分裂



翻译人: 刘伟 inewway@163.com

Ide S, Shiomi K, Mochizuki K, et al. Split Philippine Sea plate beneath Japan[J]. Geophysical Research Letters, 2010, 37(21). <https://doi.org/10.1029/2010GL044585>

摘要: 菲律宾海板块俯冲到日本下方的形状是理解日本发生地震和火山活动的一个关键因素。我们认为由于菲律宾海板块俯冲方向的突然改变而导致板块的弹性变形和应力在残留洋脊附近累积,致使菲律宾海板块沿残留洋脊发生分裂。菲律宾海板块的这种分裂形状与接收函数图像、深震源分布、板内地震的地震活动性和震源机制以及地下水中氦同位素异常比值的分布一致。菲律宾海板块的运动历史可以解释近 2-4 Ma 时期日本西部的活动构造。火山前缘的位置和板块分裂控制了流体在地壳中上升的位置,而这些流体是大地震和火山产生的原因。

ABSTRACT: The shape of the Philippine Sea Plate subducting beneath western Japan is a crucial factor in understanding earthquakes and volcanic activity. We propose that the subducted plate was split along an extinct ridge due to an abrupt change of subduction direction, followed by elastic deformation of the plate and an accumulation of stress near the ridge. This shape is consistent with receiver function images, the distribution of deep tremor sources, the seismicity and focal mechanisms of intraplate earthquakes, and the distribution of anomalous ratios of helium isotopes in ground water. The movement history of the plate can explain active tectonics in western Japan in the last 2–4 Ma. The location history of the volcanic front and the tear control where fluids ascend in the crust, and these fluids are responsible for the generation of large earthquakes and volcanoes.

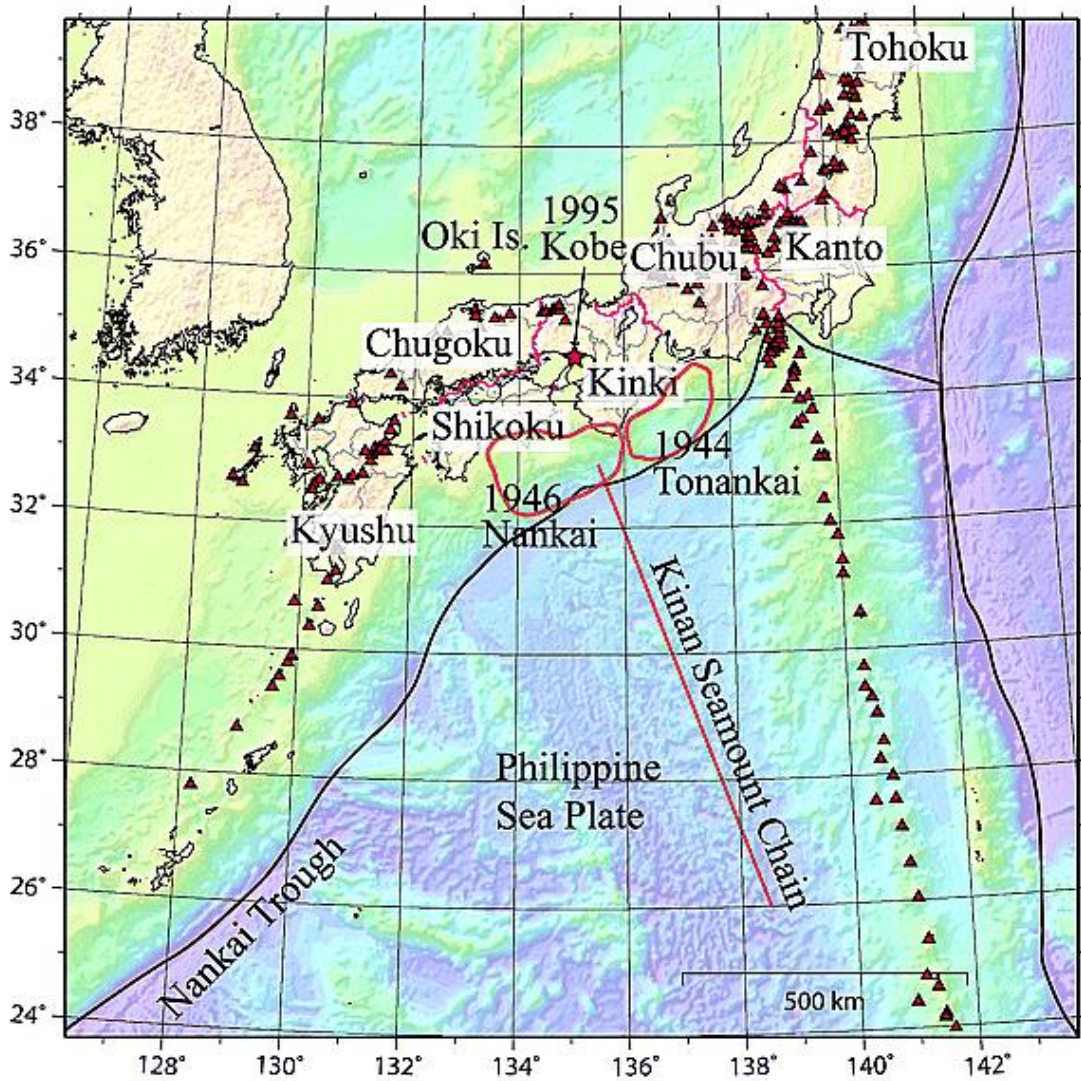


Figure 1. Bathymetry around western Japan from ETOPO1 [Amante and Eakins , 2009]. The regions in Japan are separated by purple lines. The straight red line shows the location of the Kinan Seamount Chain, which is an extinct ridge. Red triangles are Quaternary volcanoes [Committee for Catalog of Quaternary Volcanoes in Japan , 1999]. The source areas of two megathrust earthquakes, the 1944 Tonankai, and the 1946 Nankai, are shown by the curved red lines.

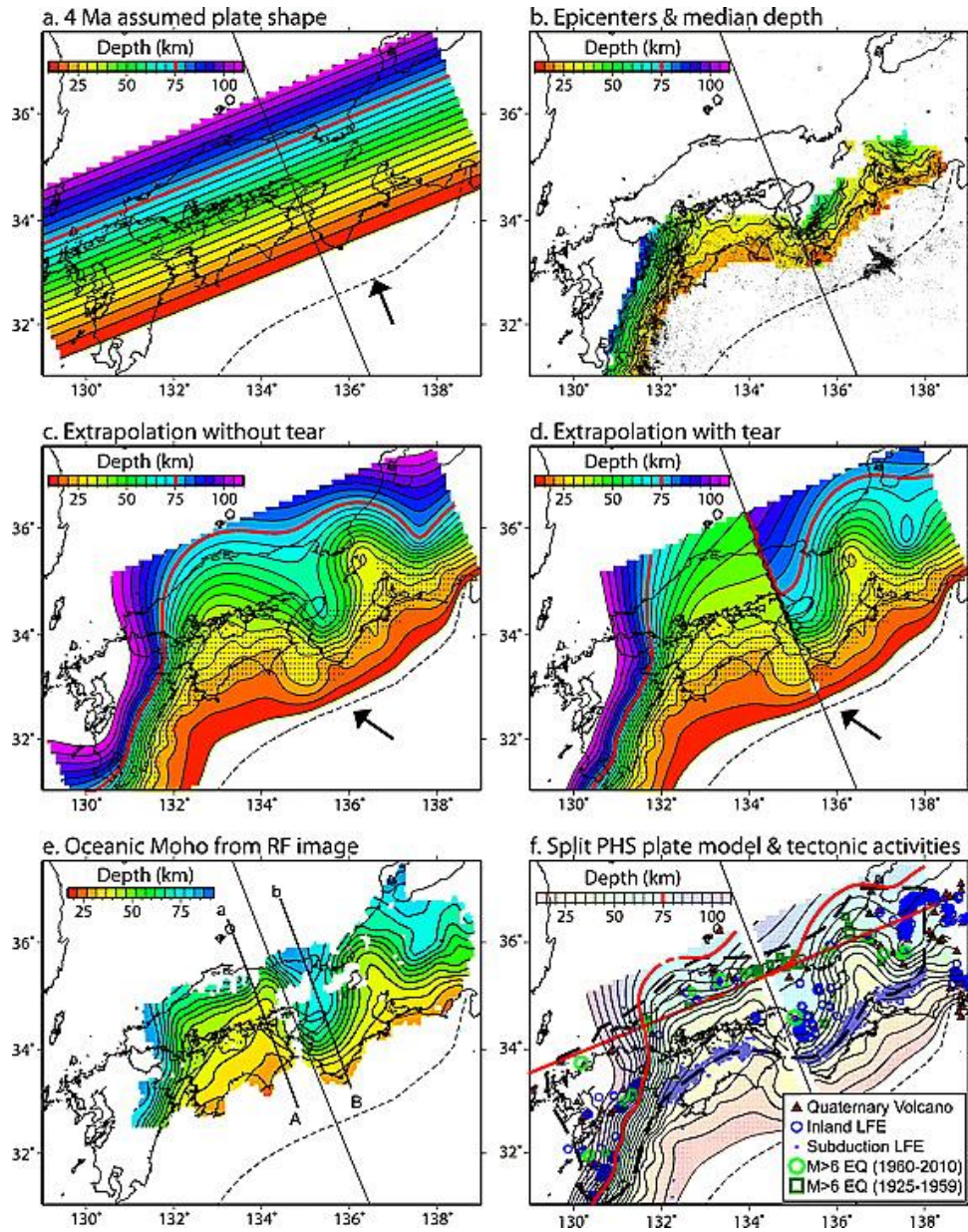


Figure 2. (a) A hypothetical plate shape at 4 Ma, before the change of plate subduction direction. An elastic slab is simply dipping in the direction of plate subduction, parallel to the ridge the location of which is shown by a black line. The contour of 75 km is shown in red to indicate the approximate location of the volcanic front. (b) Seismicity data used in this study and the spatial change of the median depth. Dots are epicenters for earthquakes deeper than 25 km. The colored contours are for a plane that is 7 km above the median depth. (c) Extrapolated surface of the plate without tear. (d) Extrapolated surface of the plate with a tear in the same position as the extinct ridge. (e) Depth contours for the oceanic Moho within the subducting PHS Plate estimated from RF image. RF images are shown along two lines a-A and b-B in Figure 4. (f) Surface of the final split PHS plate model. Symbols are Quaternary volcanoes, LFEs, and large ($M > 6$) earthquakes in the area surrounded by a thick dashed curve. We define the southern edge of this area in terms of LFEs on the subducting plate [Katsumata and Kamaya, 2003; Shelly et al., 2006], thus excluding the possible effects of megathrust earthquakes in the Nankai subduction zone. The discontinuous curved red line represents the 75 km depth contour and the straight red line is the one in Figure 2a.

6. 阿拉斯加中南部 Castle Mountain Fault 的地球物理研究



翻译人：曹伟

F.D. Ziwu, D.I. Doser and S.M. Schinagel, A geophysical study of the Castle Mountain Fault, southcentral Alaska[J], Tectonophysics 2020, <https://doi.org/10.1016/j.tecto.2020.228567>

摘要：Castle Mountain Fault (CMF) 距离阿拉斯加人口最多的城市安克雷奇不到 50 公里，对于阿拉斯加中南部的 Anchorage-Matanuska-Susitna 山谷地区来说是一个重要的地震威胁。地震活动性的特征随着 CMF 的变化而变化。尽管有证据表明 CMF 的西部（149.5°和 151°W 之间）显示出晚更新世或全新世反向和右旋运动，但在过去大约 50 年的当地地震台网监测中，它一直处于地震平静状态。相反，在 149.5°W 以东的 CMF 与背景地震活动有相当大的关系，包括 5.81984Mw 的走滑萨顿地震。我们利用重磁资料，通过以往的地震反射和地震层析成像研究结果进行约束，对 CMF 的地下结构进行建模，以确定其地震变化的控制因素。我们的模型与大角度逆断层（西北侧朝上，倾角~85°~87°）作用相一致，该断层呈现出晚中生代岩石在垂向偏移了 2000-2500 米。由于数据覆盖面的限制，无法对其总的走滑运动进行估计。全新世运动在 CMF 上呈现出由低重磁值所界定的断层两侧沉积岩组成区域有关。如果大部分的垂直偏移产生于中新世以来 Yakutat 微板块与北美板块的碰撞，那么我们的结果就可以与最近的热年代学和古地震垂直滑动速率估计值相比较。Yakutat 微板块边缘的俯冲可能在空间上影响了 CMF 沿线的地震行为，而 1964 年阿拉斯加大地震的发生也在时间上影响了当地的地震活动。

ABSTRACT: The Castle Mountain Fault (CMF) lies less than 50 km from Alaska's most populous city of Anchorage and represents an important seismic hazard to the Anchorage-Matanuska-Susitna Valley region in southcentral Alaska. The character of seismicity varies along the CMF. Although the western CMF (between 149.5° and 151° W) shows evidence for Late Pleistocene or Holocene reverse and dextral movement, it has been seismically quiet over the past ~50 years of local seismic network operation. In contrast, the CMF east of 149.5° W is associated with considerable background seismicity, including the Mw 5.81984 strike-slip Sutton earthquake. We have used gravity and magnetic data, constrained with results of previous seismic reflection and seismic tomography studies, to model subsurface structure of the CMF in an effort to determine what may control the variation in its seismic behavior. Our models are consistent with a component of high angle reverse faulting (northwest side up, dip~85°to 87°) that appears to have vertically offset Late

Mesozoic rocks 2000 to 2500 m. Lack of data coverage precludes an estimate of its total strike-slip motion. Holocene movement on the CMF appears to be associated with a region where both sides of the fault consist of sedimentary rocks as defined by a gravity and magnetic low. If most of the vertical offset has occurred since the Miocene in response to collision of the Yakutat microplate with North America, then our results are comparable to recent thermochronological and paleoseismic estimates of vertical slip rates. Subduction of the edge of the Yakutat microplate appears to spatially influence seismic behavior along the CMF while the occurrence of the 1964 Great Alaska earthquake has also temporally affected local seismicity.

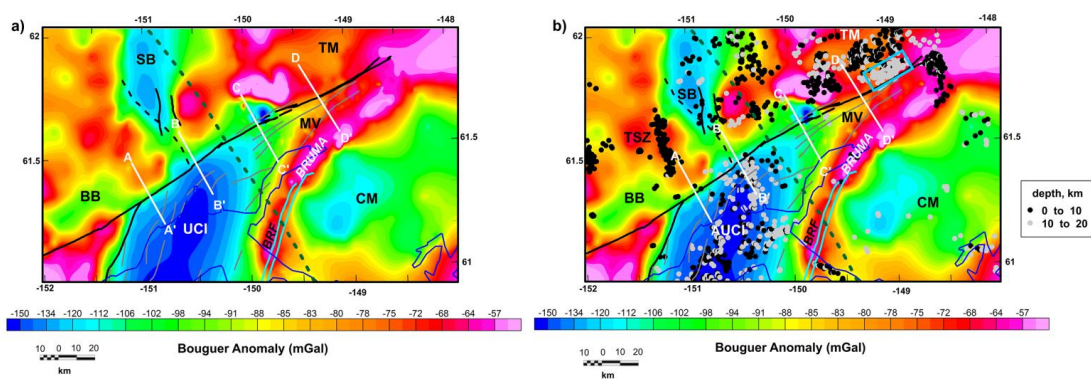


Figure 1. Simple Bouguer gravity anomaly map gridded at 1000 m. a) Faults, folds and location of edge of Yakutat microplate. b) Bouguer gravity anomaly map with relocated seismicity. Black circles are events with depths <10 km and gray circles are events with depths of 10–20 km. TSZ is the Talachultina Seismic Zone. Blue box along eastern Castle Mountain fault is the aftershock zone of 1986 Sutton earthquake

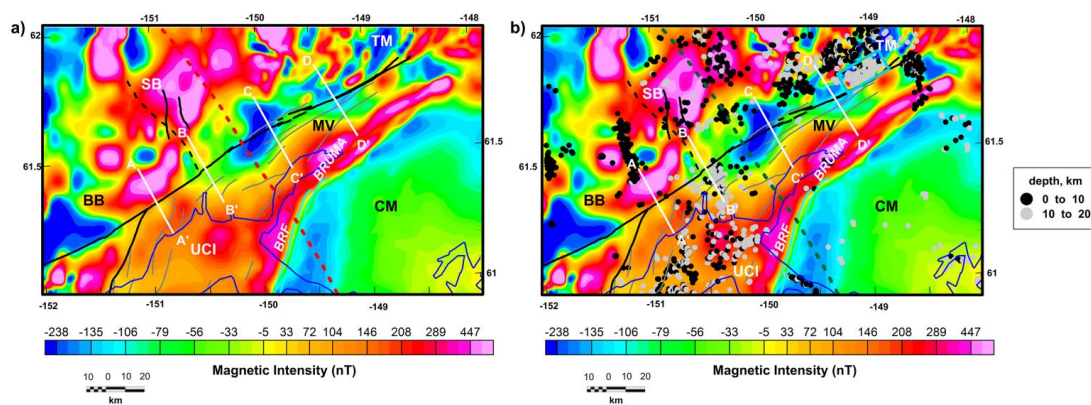


Figure 2. Total intensity aeromagnetic map gridded at 1000 m. a) Faults, folds and location of edge of Yakutat microplate. b) Magnetic anomaly map of study area with relocated seismicity.

7. 东亚降雨 $\delta^{18}\text{O}$ 与多种季风指标的关系



翻译人: 杨会会 11849590@mail.sustech.edu.cn

Wang Y Z, Hu C Y, Ruan J Y et al. *East Asian Precipitation $\delta^{18}\text{O}$ Relationship With Various Monsoon Indices [J]. Journal of Geophysical Research: Atmospheres, 2019, 125, e2019JD032282. <https://doi.org/10.1029/2019JD032282>*

摘要: 中国石笋氧同位素的变化被广泛认为记录了东亚季风的演化。然而, $\delta^{18}\text{O}$ 与季风强度的定量化校正还没有建立。为了理解 $\delta^{18}\text{O}$ 的气候意义, 我们每月测量中国和尚洞降水的 $\delta^{18}\text{O}$ 数据, 该洞穴石笋的 $\delta^{18}\text{O}$ 记录之前已经得到了。我们通过将当地的气象数据和多种季风指标进行对比, 检验了当地气候与大尺度大气环流对 $\delta^{18}\text{O}$ 的影响。结果发现雨量和温度效应都不明显, 因此认为当地气候不是 $\delta^{18}\text{O}$ 变化的主要驱动因素。在季节时间尺度上, 每月的 $\delta^{18}\text{O}$ 与所有季风指标对应, 尤其是印度季风 (IM) 和西北太平洋季风(WNPM)指标, 证明 $\delta^{18}\text{O}$ 主要响应了热带季风环流。在年际时间尺度上, $\delta^{18}\text{O}$ 与由纬向风定义的 WNPM 和 IM 季风指数呈显著的负相关, 反映了 ENSO 对 $\delta^{18}\text{O}$ 的影响。在这些季风区, $\delta^{18}\text{O}$ 与降水量之间的类似相关性进一步支持了这一发现。因为季节和年际季风变化的驱动力, 可以分别与轨道和亚轨道尺度的变化进行比较, 我们认为中国南部石笋的 $\delta^{18}\text{O}$ 由外部驱动和内部变化共同影响。太阳辐射在轨道尺度上扮演了不可避免的角色, 而海汽交互作用在亚轨道尺度上占主导。

ABSTRACT: Chinese speleothem oxygen isotope ($\delta^{18}\text{O}$) variations have been widely interpreted as recording the evolution of the Asian Monsoon. However, calibration of $\delta^{18}\text{O}$ to monsoon intensity has not yet been carried out in a quantitative way. To understand the climatic significance of $\delta^{18}\text{O}$, we measured monthly precipitation $\delta^{18}\text{O}$ data at Heshang Cave, China, where speleothem $\delta^{18}\text{O}$ records were previously obtained. We examined the influence of local climate and large-scale atmospheric circulation on the $\delta^{18}\text{O}$ by correlating to local meteorological data and various monsoon indices. We find neither a significant amount effect nor temperature effect, and therefore suggest that local climate is not the primary driver of $\delta^{18}\text{O}$ variability. On seasonal timescales, monthly $\delta^{18}\text{O}$ is significantly correlated to all monsoon indices, especially the Indian Monsoon (IM) and Western North Pacific Monsoon (WNPM) indices, proving $\delta^{18}\text{O}$ responds dominantly to the tropical monsoon circulation. On interannual timescales, there are significant negative correlations between

annual $\delta^{18}\text{O}$ and the WNPM and IM monsoon indices defined by zonal winds, reflecting the impact of the El Niño-Southern Oscillation on $\delta^{18}\text{O}$. Similar correlations between $\delta^{18}\text{O}$ and precipitation amount in these monsoon regions lend further support to this finding. As the driving force of seasonal and interannual monsoon changes can be compared to variations on orbital and suborbital scales, respectively, we argue that speleothem $\delta^{18}\text{O}$ in southern China is influenced by both external forcing and internal variability. Solar radiation plays an indispensable role on the orbital and seasonal scale $\delta^{18}\text{O}$ variations, whereas ocean-atmosphere interactions are dominant on suborbital timescales.

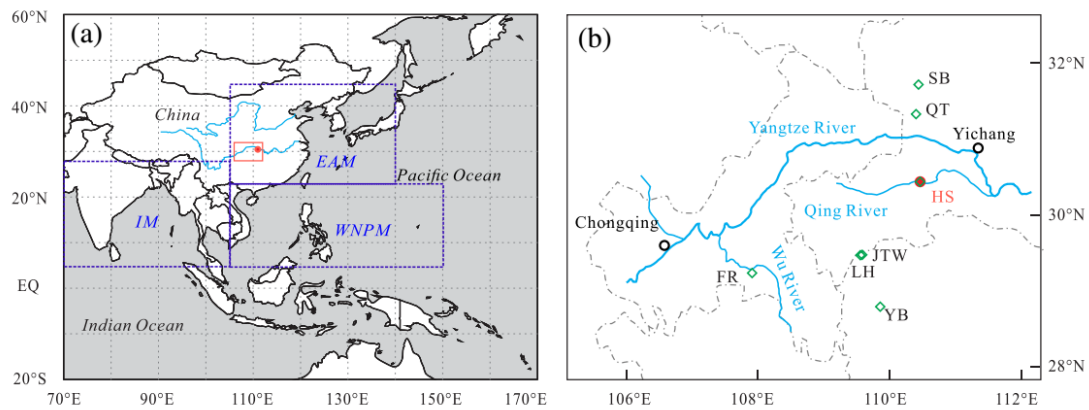


Figure 1. (a) Asian Monsoon and its subsystems. The study area and observation station HS are marked by a red square and red dot, respectively. (b) Schematic diagram of the study area. The red dot represents the location of precipitation sampling and the adjacent Heshang Cave (HS). The open diamonds represent caves that developed in neighboring regions, including Sanbao Cave (SB), Qingtian Cave (QT), Lianhua Cave (LH), Yaoba Don Cave (YB), Jintanwan Cave (JTW), and Furong Cave (FR).

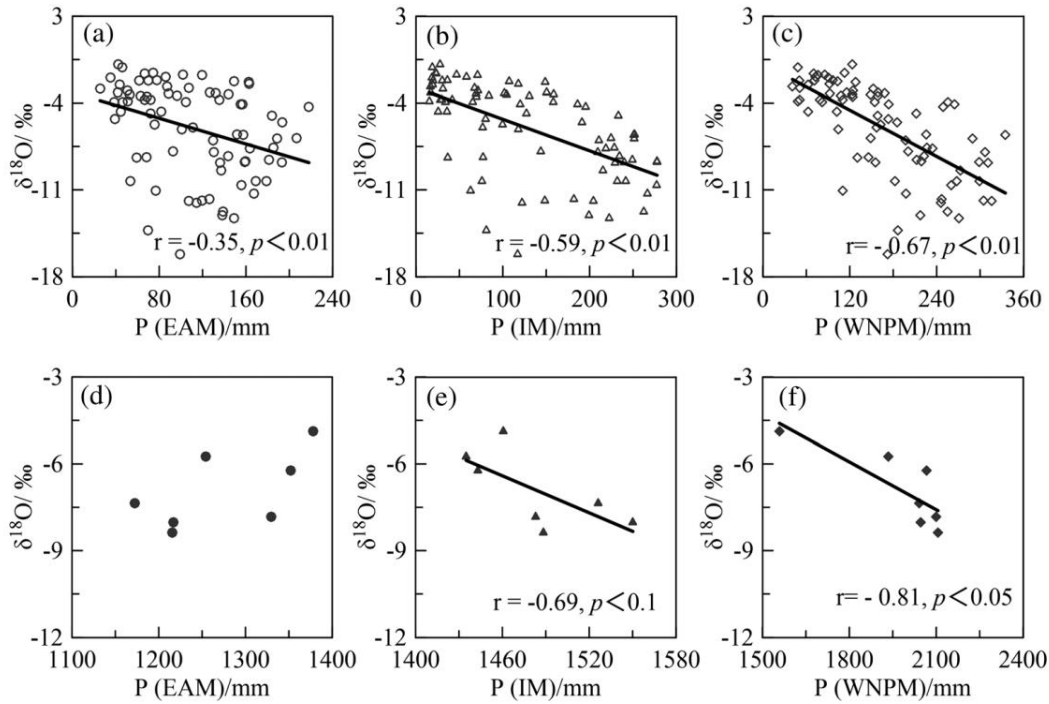


Figure 2. Correlation diagrams of HS precipitation $\delta^{18}\text{O}$ and precipitation amount in EAM (22.5° – 45° N, 105° – 140° E), IM (5° – 27.5° N, 65° – 105° E), WNPM (5° – 22.5° N, 105° – 150° E) regions (Wang et al., 2003) on seasonal and interannual timescales from May 2011 to April 2018. The first row shows the seasonal timescale correlations, the ordinates are the monthly $\delta^{18}\text{O}$, and the abscissas is the precipitation amount: (a) EAM region (hollow dots); (b) IM region (hollow triangles); (c) WNPM region (hollow diamonds). All correlations on seasonal timescale are significant at p values of <0.01 . The second row shows the interannual timescale correlations, the ordinates are the weighted average of $\delta^{18}\text{O}$, and the abscissas is the precipitation amount: (d) EAM region (solid dots); (e) IM region (solid triangles); (f) WNPM region (solid diamonds). Correlation between HS $\delta^{18}\text{O}$ and IM precipitation amount on interannual timescale is significant at p values of <0.1 , and correlation between HS $\delta^{18}\text{O}$ and WNPM precipitation amount on interannual timescale is significant at p values of <0.05 .

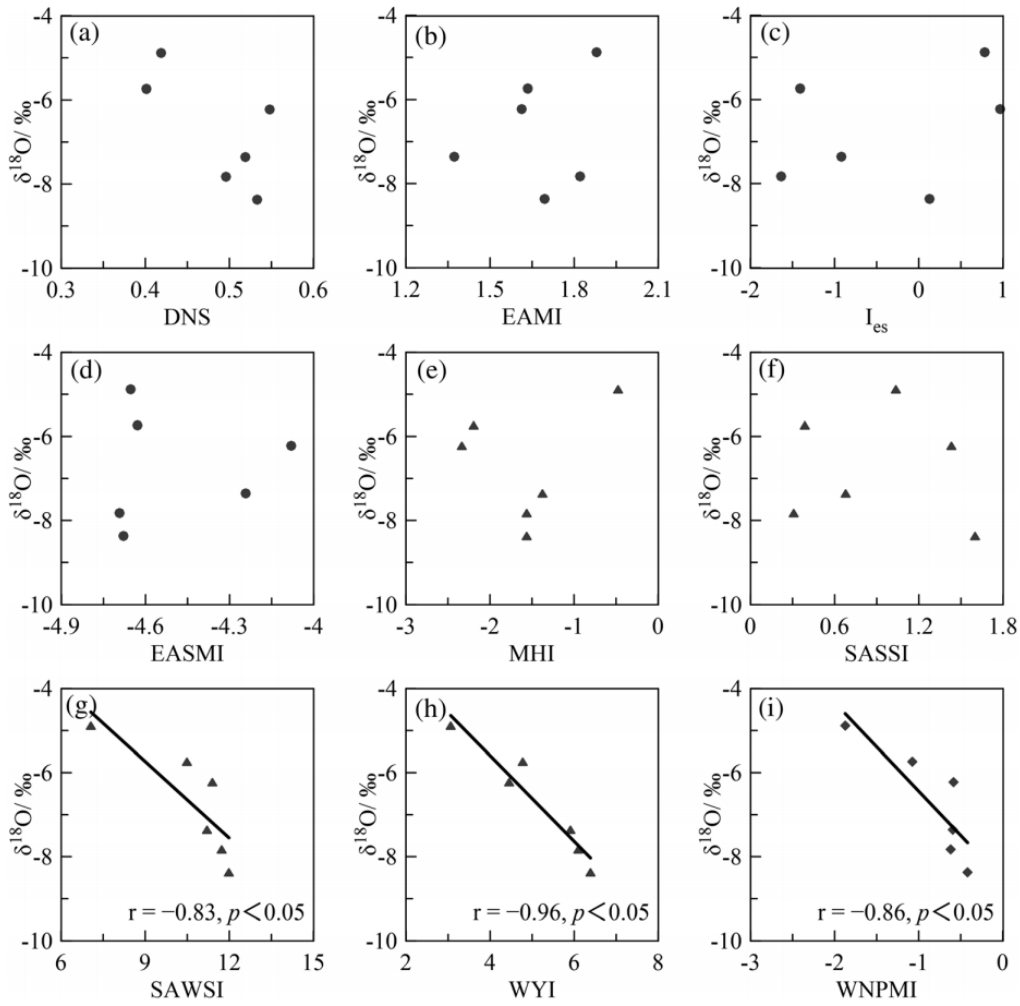


Figure 3. Correlation diagrams of the weighted average of HS precipitation $\delta^{18}\text{O}$ and nine annual monsoon indices on the interannual timescale. The ordinates are the weighted average of $\delta^{18}\text{O}$, and the abscissas are the annual monsoon indices. (a–d) EAM indices (solid dots): DNS, EAMI, I_{es} , and EASMI; (e–h) IM indices (solid triangles): MHI, SASSI, SAWSI, and WYI; (i) WNPM index (solid diamonds): WNPMI. Only correlations of SAWSI, WYI and WNPMI are significant at p values of <0.05 .

8. 微生物铁还原过程对碳酸盐沉淀的影响

翻译人: 王敦繁 dunfan-w@foxmail.com



Zeng Z, Tice M M. *Promotion and nucleation of carbonate precipitation during microbial iron reduction*[J]. *Geobiology*, 2014, 12(4):362–371.

摘要: 含铁的早期成岩碳酸盐岩胶结物在沉积岩中很常见, 它们被认为与微生物的铁还原有关。然而, 对于活跃的铁还原细胞周围的当地环境如何影响碳酸盐矿物沉淀率和成分, 我们知之甚少。以铁还原菌希瓦氏菌(*Shewanella oneidensis* MR-1)进行沉淀实验, 检测细胞在促进沉淀中的潜在作用, 并探索不同液体组成中可能产生的沉淀成分的范围。积极的铁还原细胞诱导碳酸盐矿物饱和和核沉淀在其极点。然而, 只有当钙存在于溶液中时才会发生沉淀, 这表明细胞表面通过吸附或细胞内氧化铁沉淀降低了局部亚铁浓度, 即使它们在局部升高了 pH。由此产生的沉淀是一系列热力学不稳定的富钙菱铁矿, 它们可能是形成菱铁矿、方解石甚至白云石的前体。通过改变局部 pH 值、提供成核位点和改变细胞表面周围的金属离子浓度, 铁还原微生物可以在自然沉积物中产生广泛的碳酸盐胶结物。

ABSTRACT: Iron-bearing early diagenetic carbonate cements are common in sedimentary rocks, where they are thought to be associated with microbial iron reduction. However, little is yet known about how local environments around actively iron-reducing cells affect carbonate mineral precipitation rates and compositions. Precipitation experiments with the iron-reducing bacterium *Shewanella oneidensis* MR-1 were conducted to examine the potential role of cells in promoting precipitation and to explore the possible range of precipitate compositions generated in varying fluid compositions. Actively iron-reducing cells induced increased carbonate mineral saturation and nucleated precipitation on their poles. However, precipitation only occurred when calcium was present in solution, suggesting that cell surfaces lowered local ferrous iron concentrations by adsorption or intracellular iron oxide precipitation even as they locally raised pH. Resultant precipitates were a range of thermodynamically unstable calcium-rich siderites that would likely act as precursors to siderite, calcite, or even dolomite in nature. By modifying local pH, providing nucleation sites, and altering metal ion concentrations around cell surfaces, iron-reducing microorganisms could produce a wide range of carbonate cements in natural sediments.

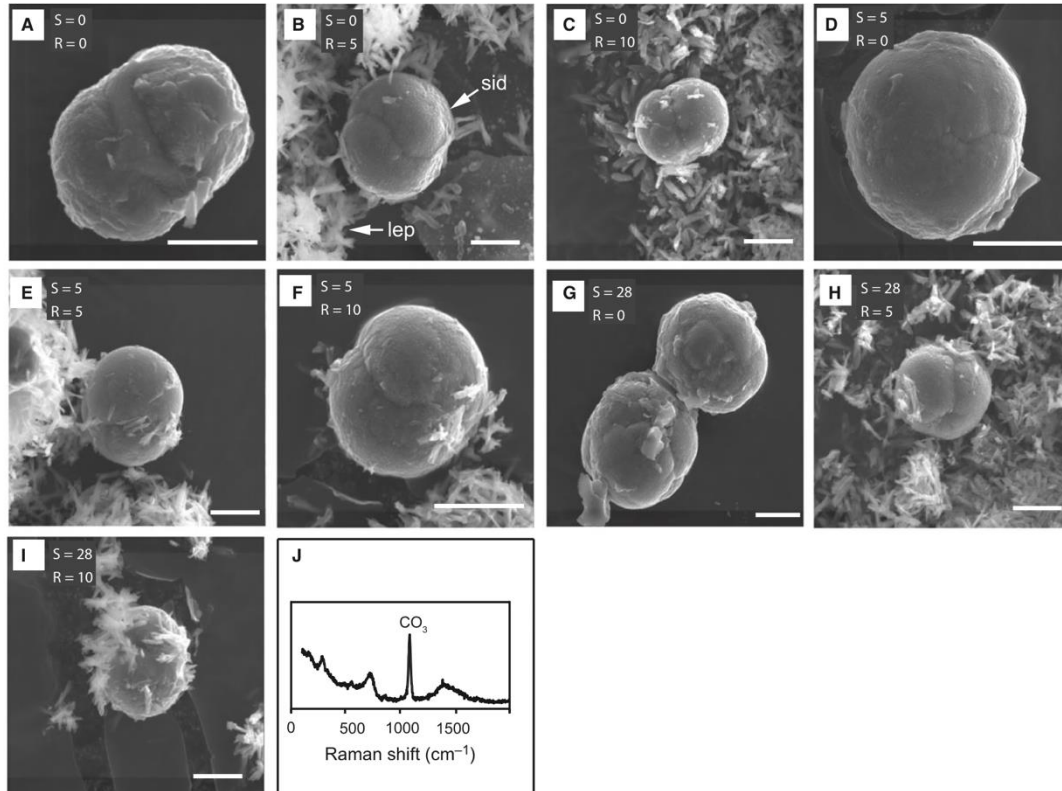


Figure 1. (A–I) Carbonate minerals precipitated during one-month-long iron reduction experiments with treatments noted. S = concentration of sulfate, R = ratio of [Mg²⁺]/[Ca²⁺], sid = siderite, and lep = lepidocrocite. Scale bars are 5 μ m. (J) Raman analysis of spherical grain.

9. Azores 群岛熔岩流序列中最后一次地磁极倒转的火山记录

翻译人: 王浩森 502691781@qq.com



Ricci J, Carlut J, Marques F O, et al. 2020. *Volcanic Record of the Last Geomagnetic Reversal in a Lava Flow Sequence From the Azores. Frontiers in Earth Science [J], 8: 13.* doi: 10.3389/feart.2020.00165

摘要: 本文介绍了来自Azores群岛的二十五个堆积熔岩流样品的古地磁和地质年代学数据, 这些熔岩流是在上一次地磁倒转过程中(马图亚山-布鲁什, M-B)形成的。通过交变磁场和/或热退磁来剥离天然剩磁的特征方向。从下到上, 方向变化显示在第一阶段呈现出反向, 随后在第二阶段呈现出过渡和正常方向的第二阶段。利用钾-氩(K-Ar)对新鲜分离的陆块进行年龄测量, 第一和第二个过渡时期的年龄分别为 768 ± 5 ka和 765 ± 5 ka (1 σ)。我们推断该序列记录了地磁场最后一次倒转, 并显示出了过渡后不久出现的回升。过渡时期比其他火山地区年轻5-15年, 但与最近为过渡期提出的天文学年龄相符。倒转的特征在于过渡期间的地磁场强弱变化, 反弹期间又出现了恢复和下降。在南大西洋和北太平洋上空发现了两个表征过渡的虚拟地磁极(VGP)。与其他M-B记录相比, 在首选位置暂未找到VGP。

ABSTRACT: We present paleomagnetic and geochronological data of twenty-five stacked lava flows from Sao Miguel Island (Azores) that were emplaced during the last geomagnetic reversal (Matuyama-Brunhes, M-B). The characteristic direction of natural remanent magnetization was isolated through alternating field and/or thermal demagnetization. From bottom to top, the directional changes display a first phase with reverse, transitional and normal directions which is followed by a second phase with transitional and normal directions. Dating by Potassium-Argon (K-Ar) of fresh separated groundmass provide ages of 768 ± 5 ka and 765 ± 5 ka (1 sigma) for the first and second transitional episodes, respectively. We infer that this sequence recorded the last reversal and reveal the presence of a rebound that occurred soon after the transition. The age of the transition is 5-15 kyr younger than at other volcanic localities, but in agreement with astronomical ages that were recently proposed for the transitional interval. The reversal is characterized by weak field intensity during the transition, a recovery phase and a subsequent decrease during the rebound. The two transitional virtual geomagnetic poles (VGPs) that characterize the transition are found above the South Atlantic and the North Pacific. When compared to other M-B records, no VGP is

found above preferred locations.

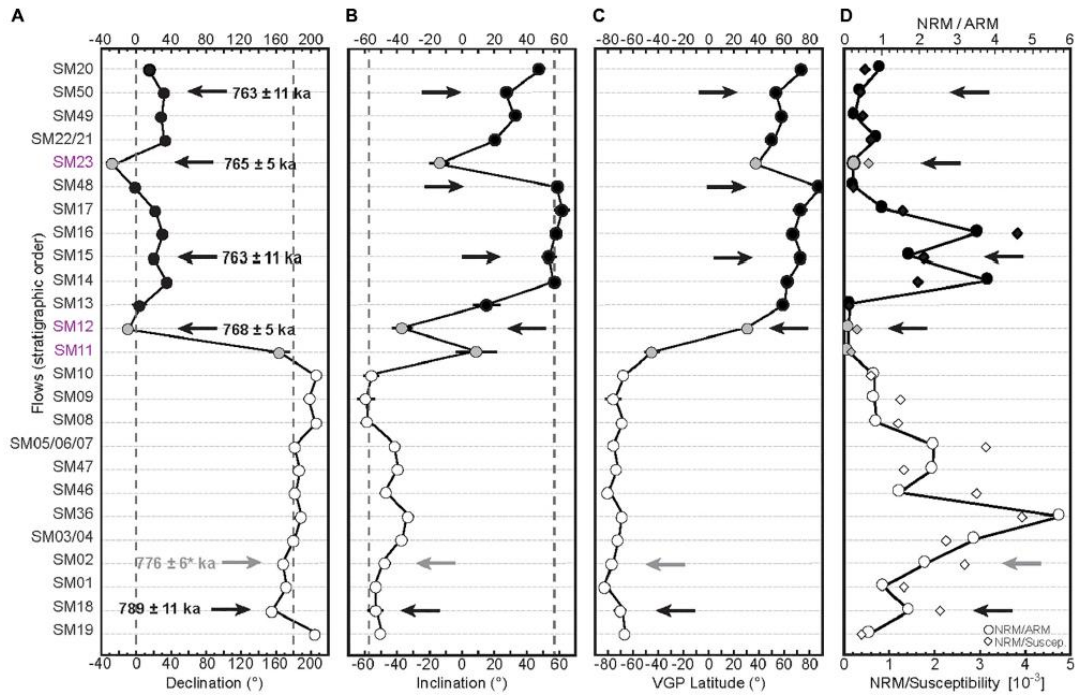


Figure 1. Mean Declination (A), inclination (B), paleolatitude of virtual geomagnetic poles (C) and relative paleointensity (D) of each flow plotted by order of appearance in the sequence. Arrow heads indicate flows with an age obtained in this study and/or from Johnson et al. (1998) (SM02).

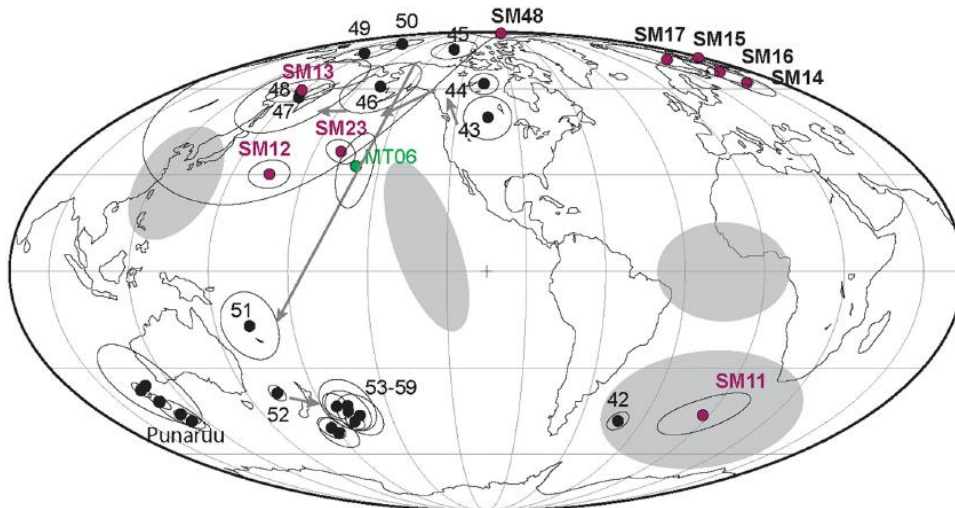


Figure 2. Virtual Geomagnetic Poles of samples dated circa 770 ka from the Maui (Coe et al., 2004), Martinique (Tantý et al., 2015), Tahiti (Chauvin et al., 1990), and Azores volcanic sequences that recorded the last reversal. Gray areas indicate the locations of the VGP groups from site U1306 sediments in North Atlantic Ocean (Channell, 2017).

10. 东亚冬季风在早全新世减弱，中晚全新世增强



翻译人：郑威 11930589@mail.sustech.edu.cn

Kang S, Du J, Wang N, et al. *Early Holocene weakening and mid-to late Holocene strengthening of the East Asian winter monsoon*[J]. *Geology*, 2020. <https://doi.org/10.1130/G47621.1>

摘要：全新世亚轨道尺度的东亚冬季风变化及其机制存在争议，部分原因是缺乏高质量的中国黄土记录。在此，我们基于中国黄土高原的三个剖面的光释光定年和粒度分析，展示了高分辨率的全新世东亚冬季风强度重建记录。东亚冬季风在早全新世（11.7-6.5 kyr B.P.）有持续减弱的趋势，在中晚全新世（自6.5 kyr B.P.始）有增强的趋势。我们认为这分别是由于北半球高纬冰量和北半球中高纬大气温度的变化导致的。我们还观察到了东亚冬季风和东亚夏季风有反相关关系。我们的发现为全新世东亚冬季风变化的争论提供了一个可靠的解释，并有助于理解东亚冬季风强度未来潜在的变化。

ABSTRACT: Sub-orbital-scale variations of the East Asian winter monsoon (EAWM) and its mechanisms during the Holocene are controversial, partly due to the lack of high-quality records from Chinese loess. Here, we present high-resolution reconstruction of Holocene EAWM intensity based on optically stimulated luminescence dating and grain-size analysis from three loess sections taken from the Chinese Loess Plateau. The EAWM showed a persistent weakening trend during the early Holocene (ca. 11.7–6.5 kyr B.P.) and a strengthening trend during the mid- to late Holocene (since ca. 6.5 kyr B.P.). We propose that this was caused by changes in high-latitude Northern Hemisphere ice volume and middle- to high-latitude Northern Hemisphere atmospheric temperatures, respectively. We also observed an anti-correlation between EAWM and East Asian summer monsoon. Our findings provide a robust solution to the debate regarding Holocene EAWM changes and contribute to the understanding of potential future variations in EAWM intensity.

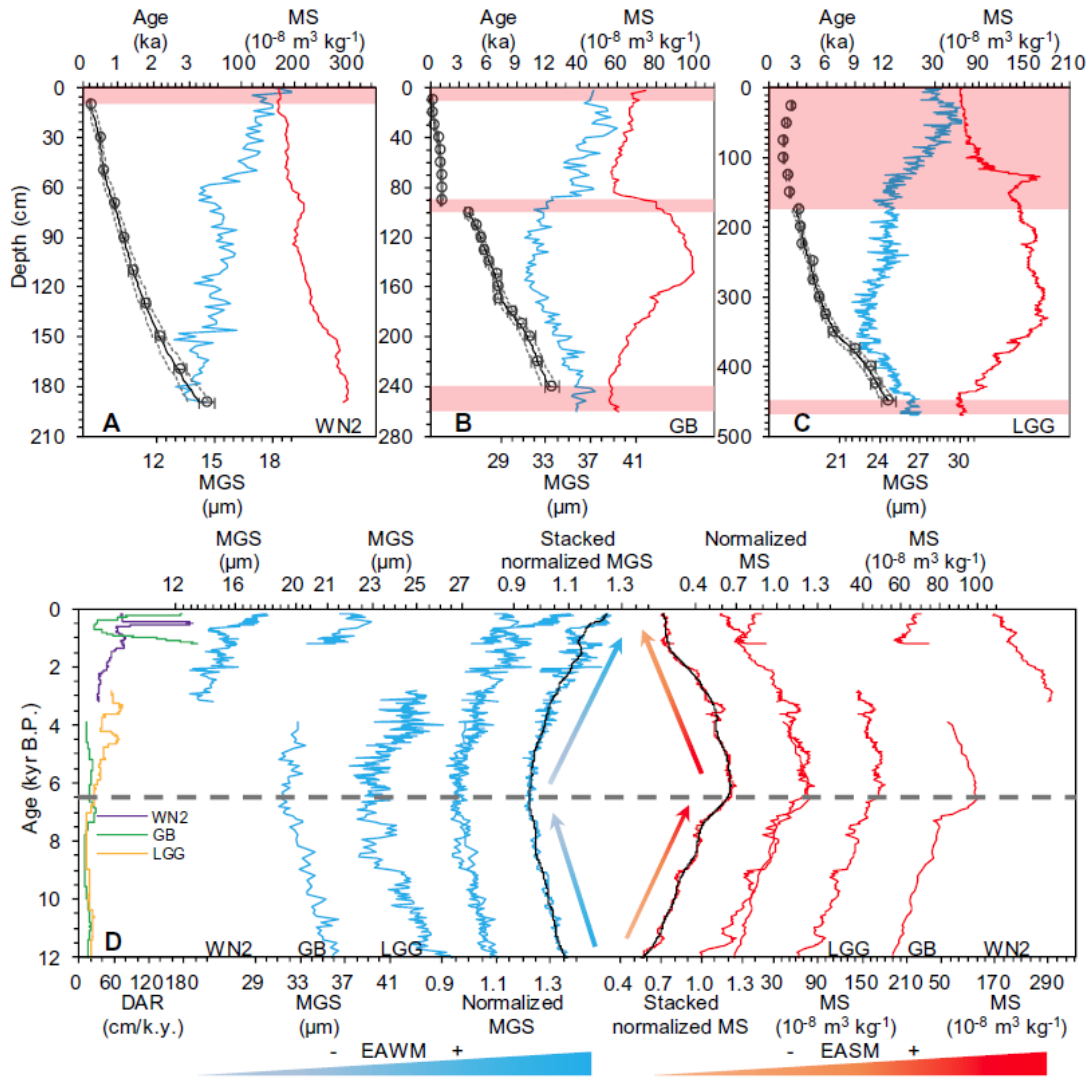


Figure 1. Chronology and proxy variations over past ~12 k.y. at WN2, GB, and LGG sections on the Chinese Loess Plateau (see Fig. 1 for locations). (A–C) Optically stimulated luminescence ages (hollow black circle), mean grain size (MGS; blue), and magnetic susceptibility (MS; red) plotted against depth. Solid black (weighted mean age) and dashed gray (95% confidence interval) curves indicate Bayesian age-depth models (see the Supplemental Material, and Fig. S9 [see footnote 1]). Pink bands indicate data excluded from paleoclimate analysis due to disturbances, hiatuses, and an absence of data within age control. (D) Dust accumulation rate (DAR), MGS, MS, normalized MGS and MS, and stacked normalized MGS and MS plotted against age. Procedures for normalization and stacking can be found in the Supplemental Material. Black solid curves indicate 1 k.y. smoothing. Blue- and red-gradient arrows and wedges indicate changing trends of the East Asian winter monsoon (EAWM) and East Asian summer monsoon (EASM) intensity. Thick gray horizontal dashed line denotes the shift in the EAWM and EASM trends at ca. 6.5 kyr B.P.